


Integer multiplier for the orbital angular momentum of light using a circular-sector transformationSatoru Takashima, Hirokazu Kobayashi *, and Katsushi Iwashita*Graduate School of Engineering, Kochi University of Technology, 185 Tosayamada-cho, Kochi 782-8502, Japan*

(Received 28 February 2019; published 13 December 2019)

This paper describes an integer multiplier for the light orbital angular momentum (OAM) through circular-sector transformations, whereby the cross-sectional circular shape of the OAM mode is geometrically transformed to circular-sector shape. Our method can be simply understood in complex function theory and the transformation process can be visualized as unwrapping a Riemann surface, including multiple sheets into a single sheet. The conversion accuracy is significantly better than the previous method because our method uses single-step geometric transformation. Our method has strong potential for the spatial mode manipulation of OAM and other useful spatial modes.

DOI: [10.1103/PhysRevA.100.063822](https://doi.org/10.1103/PhysRevA.100.063822)**I. INTRODUCTION**

It is more than 20 years since Allen *et al.* recognized that light waves with an azimuthal phase term $\exp(il\theta)$ are associated with photons that have a quantized intrinsic orbital angular momentum (OAM) $l\hbar$, where θ is the azimuthal angle on the beam cross section and the integer l is the topological charge [1]. The unlimited range of the topological charge l brings a new degree of freedom with an unbounded state space for light waves, and hence the mode of the OAM has become a useful tool in numerous applications [2], such as spatial mode multiplication [3,4], microscopy [5], optical tweezers [6], high-dimensional entanglement [7,8], and quantum cryptography [9,10].

The creation or manipulation of OAM modes can be accomplished using various optical elements, e.g., spiral phase plates [11,12], computer-generated holograms [13,14], q plates [15,16], conical mirrors [17,18], and metamaterials or metasurfaces [19–21]. However, these conventional methods can only perform shift operations (additive or subtractive operations) on the OAM mode. In addition to shifting the OAM mode, it would be extremely useful to be able to multiply the OAM state for some applications, such as the multiplicative creation of higher order OAM modes, optical switching and routing operations [22], and optical information processing [23]. Although an OAM multiplier combined with frequency up-conversion has been achieved using nonlinear second harmonic generation [24–26], this is unlikely to be sufficiently efficient for many practical applications.

Recently, another sophisticated implementation of OAM multiplication was reported using log-polar geometric transformations [27,28], which had previously been exploited for OAM mode sorting [29–31]. In the log-polar OAM multiplier, the annular shape of the OAM modes is unwrapped to N copies of the rectangular shape with an N -fold linear phase, followed by rewrapping to the annular shape. This method has the excellent property that, in principle, lossless and reversible

conversion is possible. However, there is also a fundamental problem, as the accuracy of the OAM multiplication decreases because of experimental difficulties in implementing multiple log-polar geometric transformations and the loss of the periodic boundary condition along the azimuthal angle of the OAM modes.

In this paper, we consider an essentially different approach that avoids the limitations of the log-polar OAM multiplier. We propose and experimentally demonstrate that *circular-sector transformation*, i.e., mapping the circular to the circular-sector shape, can be exploited as an OAM multiplier. The proposed OAM multiplier is based on the parallel implementation of multiple circular-sector transformations using the double-phase hologram technique [32,33]. Our method enables highly accurate and highly efficient OAM multiplication with a simple setup and single-step geometric transformation, without loss of the azimuthal periodic boundary condition. The theoretical predictions are verified by numerical simulations and experiments.

The remainder of this paper is organized as follows. In Sec. II, we briefly introduce geometric transformation or coordinate mapping of complex amplitude distribution, then we propose the OAM multiplier implemented by using circular sector transformations. In Sec. III, we numerically simulate conversion process of the proposed OAM multiplier. In Sec. IV, we experimentally implement the OAM doubler and tripler by using phase-only spatial light modulator and evaluate its conversion accuracy from the OAM spectrum. Summary is presented in Sec. V.

II. CIRCULAR SECTOR TRANSFORMATION AND OAM MULTIPLIER

A typical optical system for the geometric transformation or coordinate mapping, proposed by Bryngdahl [34,35], is the $2f$ configuration with two phase masks. The first is the transforming phase $\varphi(x, y)$, which implements the geometric transformation placed at the front focal plane (x, y) of the Fourier-transforming lens, and the second one is the correction phase $\Psi(u, v)$, which compensates the undesired

*kobayashi.hirokazu@kochi-tech.ac.jp

phase in the transformed beam at the Fourier plane (u, v) . In approximating the Fourier transform integral using the stationary-phase method, the point (x, y) is mapped onto the point (u, v) given by

$$(x, y) \mapsto (u, v) = \frac{f}{k}(\varphi_x, \varphi_y), \quad (1)$$

where f is the focal length of the Fourier-transforming lens, k is the wave number, and the subscripts x and y denote partial differentiation with respect to x and y , respectively. For geometric transformation applications, a mapping $(x, y) \mapsto (u(x, y), v(x, y))$ is given, and then the transforming phase $\varphi(x, y)$ is determined by solving the partial differential equations in Eq. (1) when the continuity condition $u_y = v_x$ is satisfied [36].

If the complex form of the transformation $(x, y) \mapsto (u, v)$ is an antianalytical function, i.e., $\omega = g(\bar{\zeta})$, where $\omega = u + iv$ and $\bar{\zeta} = x - iy$, then the continuity condition is satisfied by virtue of the Cauchy-Riemann differential equation for $g(\bar{\zeta})$ [37]. In the complex form, the solution of Eq. (1) can be expressed in simple form [38] as

$$\varphi(x, y) = \frac{k}{f} \text{Re} \left[\int g(\bar{\zeta}) d\bar{\zeta} \right]. \quad (2)$$

See Appendix A for details of calculation.

We now consider the circular-sector transformation for implementing the OAM multiplier. As an input beam, we assume propagating OAM mode, namely, Laguerre-Gaussian (LG) beam, of which the beam radius depends on the topological charge l . The optical complex amplitude $E_l(r, \theta)$ of LG modes with topological charge l can be expressed in polar coordinates (r, θ) as $E_l(r, \theta) \propto E_0(r)(re^{i\theta})^l \propto \zeta^l$, where the complex variable $\zeta = x + iy = re^{i\theta}$ and $E_0(r)$ is the complex amplitude of the fundamental Gaussian mode. The circular-sector transformation exploits a fractional power function as an antianalytic complex function $g(\bar{\zeta})$ expressed as

$$\omega = g(\bar{\zeta}) = \alpha \bar{\zeta}^{\frac{1}{N}}, \quad (3)$$

where the integer N corresponds to the factor of the OAM multiplier and α is a real-valued scaling constant. The geometric transformation of the OAM modes by Eq. (3) can be formulated as $\zeta^l \mapsto (\bar{\omega}/\alpha)^{Nl} \propto (\rho e^{-i\phi})^{Nl}$ on the output polar coordinate (ρ, ϕ) . Thus, the input OAM of l is multiplied by $-N$, which means that both the positive and negative multipliers can be realized depending on the sign of N . Note that the fundamental Gaussian amplitude $E_0(r)$ is also geometrically converted and becomes a super-Gaussian function. However, using the appropriate spatial low-pass filter, the super-Gaussian function can be approximated as a fundamental Gaussian function.

The complex fractional power function in Eq. (3) has a branch point of order N at the origin and is an N -valued function. Thus, the input polar coordinates (r, θ) are mapped onto the N points on the output polar coordinates, $(\rho, \phi) = (\alpha r^{\frac{1}{N}}, -\frac{\theta + 2n\pi}{N})$, where the integer $n = 0, \dots, N - 1$. As shown in Fig. 1, each coordinate mapping with a particular value of n converts the circular shape of the input OAM mode to the circular-sector shape at a different azimuthal position. If all N circular-sector transformations occur

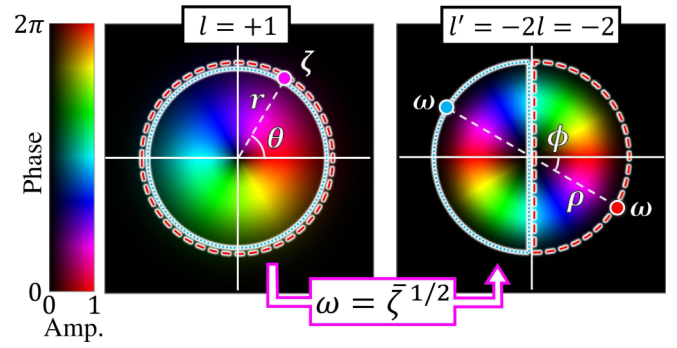


FIG. 1. Principle of integer multiplication of OAM using circular-sector transformations with $N = 2$ (OAM doubler). The input plane $\zeta = re^{i\theta}$ is mapped onto the output plane $\omega = \rho e^{i\phi}$ associated with the complex fractional power function $\omega = g(\bar{\zeta}) = \bar{\zeta}^{\frac{1}{2}}$. The red dashed and blue dotted circular shapes are mapped onto the semicircular shapes at opposite azimuthal positions by two different circular-sector transformations.

simultaneously, the input OAM is multiplied by $-N$ in the output. From Eqs. (2) and (3), the transforming phase $\varphi_n(r, \theta)$ for the n th circular-sector transformation can be calculated as

$$\varphi_n(r, \theta) = \frac{\alpha k N r^{1+\frac{1}{N}}}{f N + 1} \cos \left[\frac{(N + 1)\theta + 2n\pi}{N} \right]. \quad (4)$$

The required complex amplitude modulation for the parallel implementation of the N circular-sector transformations is given by

$$A(r, \theta) e^{i\varphi(r, \theta)} = \frac{1}{N} \sum_{n=0}^{N-1} e^{i\varphi_n(r, \theta)}, \quad (5)$$

where $A(r, \theta)$ and $\varphi(r, \theta)$ represent the normalized amplitude and phase distribution, respectively. Among many methods to implement Eq. (5) with single-phase-only spatial light modulator (SLM) [39,40], we exploit the double-phase hologram technique [32,33], whereby the required phase $\Phi(r, \theta)$ is formulated as

$$\Phi(r, \theta) = \varphi(r, \theta) + \Pi_{\pm} \cos^{-1} A(r, \theta), \quad (6)$$

where $\Pi_{\pm} = (-1)^{n+m}$ with the x - and y -directional pixel numbers n and m of the SLM is a spatially periodic function that returns values of $+1$ or -1 , like a two-dimensional binary grating (checkerboard pattern). The complex amplitude modulation in Eq. (5) can be accomplished by applying a spatial low-pass filter to extract the zeroth-order diffraction component from the product of the input OAM modes and the phase mask $\Phi(r, \theta)$. See Appendix B for details.

Finally, the undesired phase factor of the transformed complex amplitude is compensated by the correction phase $\Psi(\rho, \phi)$ calculated under the stationary-phase method [34,36]. As the circular-sector shapes do not overlap, the correction phase can be formulated as the following single continuous function:

$$\Psi(\rho, \phi) = \frac{k}{f} \left(\frac{\rho}{|\alpha|} \right)^N \frac{\rho \cos[(N + 1)\phi]}{N + 1}. \quad (7)$$

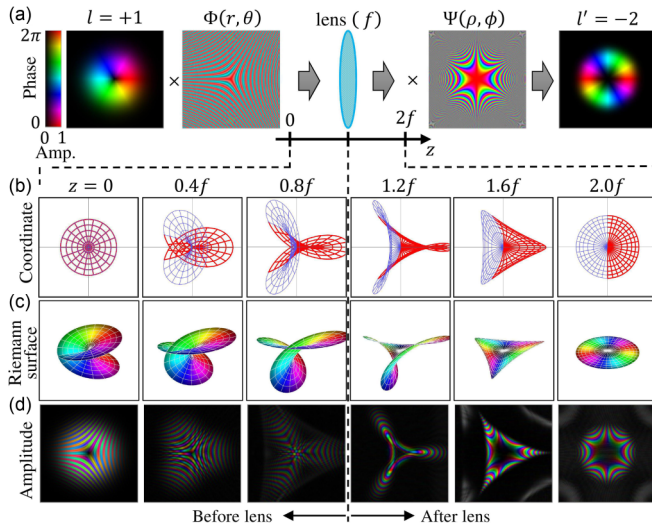


FIG. 2. Numerical simulation of conversion process of OAM multiplication with $N = 2$ (OAM doubler). (a) Two required phase masks, Ψ and Φ , for the OAM doubler and output complex amplitude calculated by fast Fourier transform. (b) Ideal conversion process of the two polar coordinates (red thick and blue thin lines) by different circular sector transformations. (c) Conversion process of Riemann surface. (d) Conversion process of complex amplitude of the input OAM mode calculated by Fresnel diffraction integral.

III. NUMERICAL SIMULATION

In this study, we numerically and experimentally demonstrate the negative OAM multiplier ($N > 0$). Figure 2 shows the results of numerical simulations for the OAM doubler. Figure 2(a) presents the simulation result obtained by calculating the fast Fourier transform of the input OAM modes with $l = +1$ multiplied by the transforming phase. After compensating the undesired phase by $\Psi(\rho, \phi)$, the input OAM is doubled as $l' = -2l$. Figure 2(b) illustrates the ideal conversion process of the polar coordinate system during propagation inside the $2f$ system. The polar two coordinates (red thick and blue thin lines) are geometrically transformed by different circular-sector transformations with $n = 0$ and $n = 1$, resulting in a semicircular shape at opposite azimuthal positions. Using the double-phase hologram $\Phi(r, \theta)$ in Eq. (6), these two coordinate transformations occur simultaneously, and thus the two coordinates do not break the periodic boundary condition along the azimuthal angle. From the viewpoint of complex function theory, the OAM multiplier geometrically unwraps the Riemann surface with multiple sheets for the complex fractional power function to a single sheet, as shown in Fig. 2(c). Figure 2(d) shows the conversion process of the complex amplitude obtained by calculating the Fresnel diffraction in the angular spectrum domain. After propagation over a distance of $z = 2f$, the optical amplitude distribution has an annular shape but is accompanied by an undesired phase, which is compensated by the correction phase $\Psi(\rho, \phi)$.

IV. EXPERIMENT

The experimental setup is shown in Fig. 3. A light wave irradiated from a single-mode fiber pigtailed laser diode with

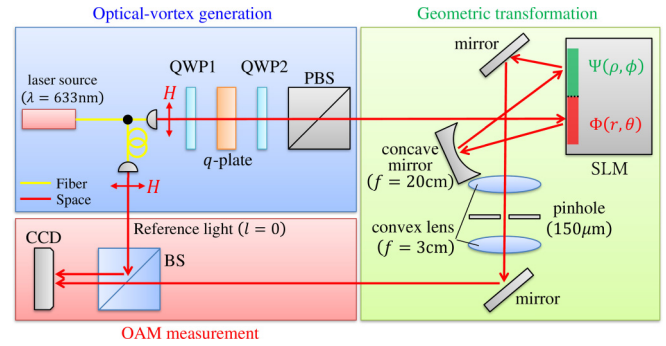


FIG. 3. Schematic of the experimental setup. BS, PBS, and QWP denote beam splitter, polarization BS, and quarter wave plate, respectively.

a wavelength of 635 nm is split into two paths by the fiber coupler, one for preparing the OAM modes and the other for the reference beam. The OAM modes ($-2 \leq l \leq 2$) and the balanced superpositions of the positive and negative OAM modes are generated from the 2.5-mm-radius collimated Gaussian beam using a q -plate device with a topological charge of $q = \frac{1}{2}$ or 1.

For the circular sector transformations, the two required phase masks $\Phi(r, \theta)$ and $\Psi(\rho, \phi)$, with the parameter $\alpha = 0.025\text{ m}^{1/2}$ for the OAM doubler and $\alpha = 0.0092\text{ m}^{2/3}$ for the OAM tripler, are prepared on the halves of the single SLM. The input OAM mode subjected to the transforming phase $\Phi(r, \theta)$ is Fourier transformed in the $2f$ configuration via reflection by the concave mirror with focal length $f = 200\text{ mm}$, followed by compensation with $\Psi(\rho, \phi)$. (In the actual experiments, a linear blazed grating phase was included in the transforming phase.) Finally, the spatial filter composed of two lenses and a pinhole extracts the first-order diffraction component, thus achieving complex amplitude modulation in Eq. (2) and reducing the undesired diffraction noise.

In the OAM measurement stage, the intensity distributions of the transformed beam and its interferograms with the reference beam are observed by a CCD camera. To verify whether the desired OAM multiplication can be implemented, the complex amplitude distribution is reconstructed from the interferogram using the angular spectrum method [41]. See Appendix C for details.

Figure 4 shows the experimentally obtained intensity distributions of the input, doubled, and tripled OAM modes. The input OAM modes with $l = \pm 1, \pm 2$ represent balanced superpositions of $+l$ and $-l$, with $l = 1, 2$, in which the intensity distribution displays $2|l|$ intensity maxima or “petals” along the azimuthal angle. As shown in the second and fourth columns in Fig. 4, we can successfully obtain a geometric transformation resulting in $2N|l|$ petals while maintaining highly accurate rotational symmetry and high visibility. For the single OAM mode with $l = +1, +2$, the annular intensity distribution is as shown in the first and third columns of Fig. 4.

Figure 5 shows the complex amplitude distributions extracted from the interferogram of the input OAM modes ($-2 \leq l \leq 2$) and of the transformed modes given by the OAM doubler and tripler. As expected, the azimuthal phase variation in the input OAM modes becomes doubled or tripled

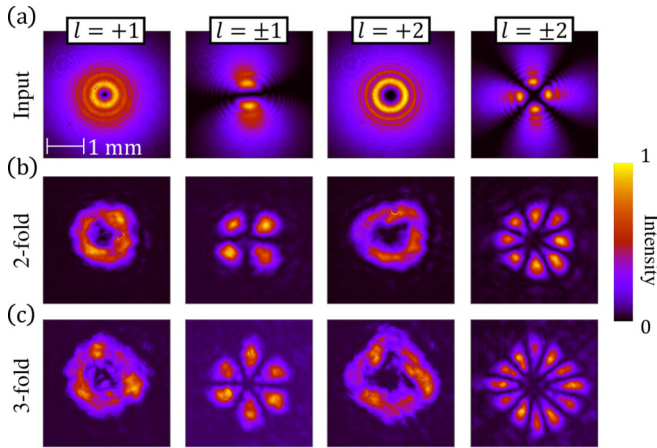


FIG. 4. Intensity distribution of (a) input, (b) twofold, and (c) threefold OAM modes obtained experimentally by geometric transformation.

and has a negative sign. In the case of the fundamental Gaussian input ($l = 0$), its phase structure remains almost unchanged.

Finally, we confirm the accuracy of the OAM multiplier by calculating the OAM spectrum from the optical complex amplitude in Fig. 5 (see Appendix D for details of calculations). Figures 6(a) and 6(b) show the output OAM spectra of the OAM doubler and tripler, respectively, in which the vertical axis shows the intensity ratio of a particular OAM mode to all OAM modes within the topological charge $-10 \leq l \leq 10$. The ratio of the desired OAM mode reaches almost 70% for the OAM doubler and almost 50% for the OAM tripler, and is more than four times the ratio of undesired other OAM modes, even for the OAM tripler. Figure 6(c) shows the averaged OAM (filled circles and filled squares) and its standard deviation (error bar) calculated from the OAM spectra in Figs. 6(a) and 6(b). There is almost no overlap between each output OAM mode within the range of one standard deviation.

We think that the reduction in transformation accuracy is due to technical issues, especially inconsistency between numerical parameter k/f in required phase holograms and

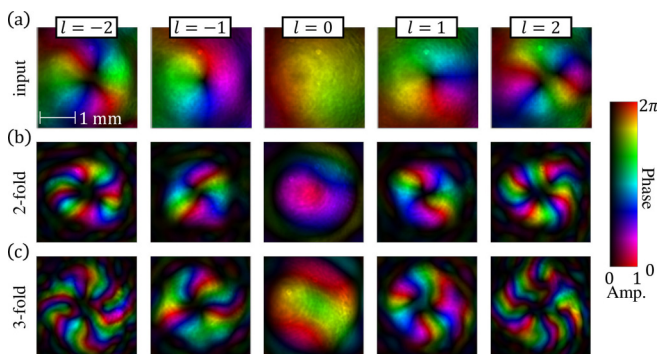


FIG. 5. Complex amplitude distribution obtained experimentally after twofold and threefold OAM multiplication. Complex amplitude distribution of (a) input, (b) twofold, and (c) threefold OAM beams.

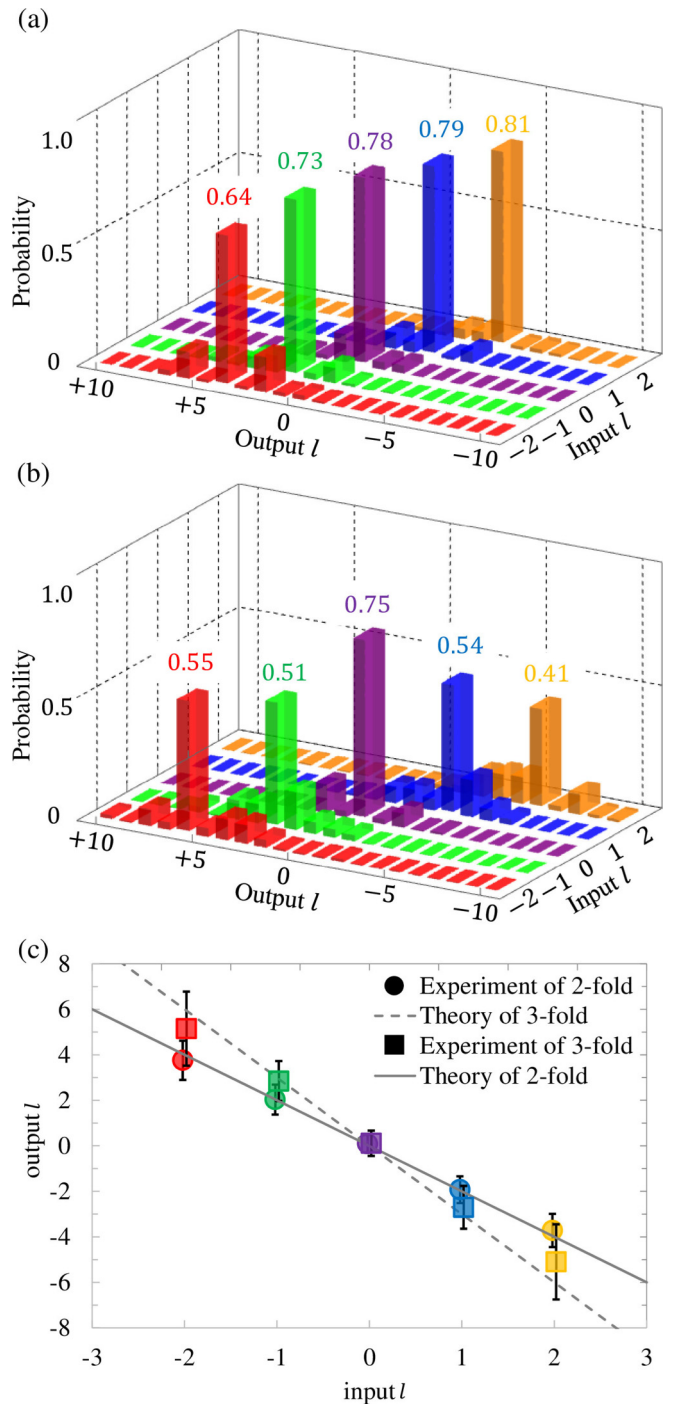


FIG. 6. Experimental results of OAM mode analysis. Probability distribution of OAM with (a) twofold and (b) threefold OAM multiplication results. (c) Average of the OAM and its standard deviation. Error bars show standard deviations of the OAM spectra in panels (a) and (b).

ratio of actual wave number k divided by focal length f of the concave mirror. Propagation distance error in the $2f$ system and aberration of the concave mirror also contribute to the reduction in transformation accuracy. It should be noted that the OAM tripler is more sensitive to these technical errors,

because it needs to make a larger deformation in the complex amplitude distribution.

Although there were some technical issues described above, the conversion accuracy of the proposed OAM multiplier is significantly improved over that of the log-polar OAM multiplier. This is obvious from a comparison of the experimental results in Fig. 6 with those for the log-polar OAM multiplier [27,28]. The improvement is the result of maintaining the periodic boundary condition under the geometric transformation and simplifying the experimental setup with a single SLM. The drawback of the proposed method is that it suffers an inevitable intensity loss because of the complex amplitude modulation in Eq. (5). The conversion efficiency of the double phase hologram for OAM multiplier is limited by $1/|N|$. However, this drawback can be overcome by using other implementation of multiple circular-sector transformations, such as the phase-only hologram $e^{i\varphi(r,\theta)}$ [42]. We believe further improvement of the efficiency and the accuracy can be achieved by multiple passive phase elements or some other sophisticated implementation. See Appendices E and F for detailed discussion about theoretical efficiency and accuracy of OAM multiplier.

V. SUMMARY

In summary, we have proposed a method for OAM multiplication through the parallel implementation of multiple circular-sector transformations. First, we introduced a general solution for the geometric transformation in complex form and then derived the circular-sector transformations by exploiting a complex fractional power function as a coordinate mapping. From the viewpoint of complex function theory, we visualized the transformation process as unwrapping a Riemann surface, including multiple sheets into a single sheet. The theoretical predictions have been experimentally demonstrated, verifying significant improvement in conversion accuracy for the OAM doubler and tripler when compared with the previous method. We expect the proposed method to be applicable to the highly accurate fractional multiplication and division of the OAM. Moreover, our scheme can be generalized to other sophisticated geometric transformations induced by multivalued complex functions. It offers great potential for the spatial mode manipulation of the OAM and other useful spatial modes.

Note added. Recently, sophisticated implementation of an OAM multiplier based on circular-sector transformation has been reported by Ruffato *et al.* [42].

ACKNOWLEDGMENTS

The authors acknowledge G. Bateson and G. Ruffato for fruitful discussion. This work was supported by the Matsuo Foundation, Research Foundation for Opto-science and Technology, and Japan Society for the Promotion of Science (JSPS) KAKENHI (Grant No. 18K14151).

APPENDIX A: STATIONARY PHASE METHOD FOR $2f$ CONFIGURATION AND ITS COMPLEX REPRESENTATION

Here we describe stationary phase method for approximating Fresnel diffraction integral in $2f$ system. When the input complex amplitude (scalar electric field) $E_{\text{in}}(\mathbf{r})$ at the incident plane $\mathbf{r} = (x, y)$ is subjected to the transforming phase $\varphi(\mathbf{r})$ and propagated along the z direction in a $2f$ system, the complex amplitude $E_{\text{out}}(s, z)$ on the plane $s = (u, v)$ at the distance z is calculated by Fresnel diffraction integral as follows:

$$E_{\text{out}}(s, z) = \frac{e^{ikz}}{i\lambda z} \int E_{\text{in}}(\mathbf{r}) e^{i\varphi(\mathbf{r})} e^{i\frac{k}{z}|\mathbf{r}-s|^2} d\mathbf{r}, \quad (\text{A1})$$

where k is the wave number and λ is the wavelength. Next, consider propagation of the light wave after passing through the Fourier transforming lens with the focal length of f placed at $z = f$. When the total propagation distance is z , the complex amplitude after the lens can be calculated as

$$E_{\text{out}}(s, z) = \frac{e^{ikz}}{i\lambda f} \int E_{\text{in}}(\mathbf{r}) e^{i\varphi(\mathbf{r})} \times \exp\left[-i\frac{k}{f}\left\{s \cdot \mathbf{r} - \left(1 - \frac{z}{2f}\right)|\mathbf{r}|^2\right\}\right] d\mathbf{r}. \quad (\text{A2})$$

When $z = 2f$, Eq. (A2) becomes

$$E_{\text{out}}(s, 2f) = \frac{e^{ikz}}{i\lambda f} \int E_{\text{in}}(\mathbf{r}) e^{i\varphi(\mathbf{r})} \exp\left(-i\frac{k}{f}s \cdot \mathbf{r}\right) d\mathbf{r} \quad (\text{A3})$$

$$\propto \mathcal{F}[E_{\text{in}}(\mathbf{r})]\left(\frac{k}{f}s\right), \quad (\text{A4})$$

where $\mathcal{F}[\cdot]$ represents Fourier transform calculation. Equation (A4) shows that the input-output relationship of the $2f$ configuration can be formulated by Fourier transform.

The stationary phase method of determining the Fresnel diffraction integral is strictly true only in the limit of infinitely large wave number k . However, it remains an excellent approximation for appropriate large value of k (small wavelength λ). This approximation states that the only significant contributions to the integral occur at the points where the phase gradient vanishes, called the stationary phase point. In approximating Fresnel diffraction integrals of Eqs. (A1) and (A2) by the stationary phase method, the stationary phase point satisfies the following equations:

$$\nabla\varphi(\mathbf{r}) = \begin{cases} -\frac{k}{z}(\mathbf{r} - s) & \text{for } 0 \leq z \leq f \\ -\frac{k}{f}\left[(2 - \frac{z}{f})\mathbf{r} - s\right] & \text{for } f \leq z \leq 2f, \end{cases} \quad (\text{A5})$$

where $\nabla \equiv (\frac{\partial}{\partial x}, \frac{\partial}{\partial y})$ is the two-dimensional differential operator. The first and the second equations in Eq. (A5) show the stationary phase conditions before and after the Fourier transforming lens, respectively. When $z = 2f$, Eq. (A5) becomes

$$\nabla\varphi(\mathbf{r}) = \frac{k}{f}s. \quad (\text{A6})$$

For applications of geometric transformation, a mapping $\mathbf{r} = (x, y) \mapsto \mathbf{s}(\mathbf{r}) = (u(x, y), v(x, y))$ is given, and the partial differential equation in Eq. (A6) is solved for $\varphi(\mathbf{r})$. Assuming that $u(x, y)$ and $v(x, y)$ have partial derivatives in a simply connected region at the input plane, Eq. (A6) has solutions for $\varphi(\mathbf{r})$ only when the following continuity condition is satisfied,

$$\frac{\partial u}{\partial y} = \frac{\partial v}{\partial x}, \quad (\text{A7})$$

or equivalently,

$$\frac{\partial \varphi}{\partial x \partial y} = \frac{\partial \varphi}{\partial y \partial x}. \quad (\text{A8})$$

By the stationary phase method, the Fresnel diffraction integral in Eq. (A3) can be approximated as

$$E_{\text{out}}(\mathbf{s}, 2f) \simeq \frac{2\pi\sigma e^{i2kf}}{i\lambda f \sqrt{|\varphi_{xx}\varphi_{yy} - \varphi_{xy}^2|}} E_{\text{in}}(\mathbf{r}_0) \times \exp\left[i\left\{\varphi(\mathbf{r}_0) - \frac{k}{f}\mathbf{r}_0 \cdot \mathbf{s}\right\}\right], \quad (\text{A9})$$

where \mathbf{r}_0 is the stationary point, the notation $\varphi_{xx} = \partial^2\varphi/\partial x^2$, etc., is used, and σ is defined by

$$\sigma = \begin{cases} i & \text{for } \varphi_{xx} > 0, \varphi_{xx}\varphi_{yy} > \varphi_{xy}^2 \\ -i & \text{for } \varphi_{xx} < 0, \varphi_{xx}\varphi_{yy} > \varphi_{xy}^2 \\ 1 & \text{for } \varphi_{xx}\varphi_{yy} < \varphi_{xy}^2 \end{cases} \quad (\text{A10})$$

From Eq. (A9), the correction phase $\Psi(\mathbf{s})$ for compensating the undesired phase term is given by

$$\Psi(\mathbf{s}) = -\varphi(\mathbf{r}_0) + \frac{k}{f}\mathbf{r}_0 \cdot \mathbf{s}. \quad (\text{A11})$$

Now we consider the geometric transformation as the coordinate mapping in complex planes from $\zeta = x + iy$ to $\omega = u + iv$. In what follows, the complex variable ω is written as $\omega(z)$ to explicitly indicate the dependence on propagation distance z and the transforming phase is written in complex form as $\varphi(\zeta, \bar{\zeta})$, where $\bar{\zeta} = x - iy$. Then, the stationary phase condition in Eq. (A5) can be given in complex form as follows:

$$\frac{\partial \varphi(\zeta, \bar{\zeta})}{\partial \bar{\zeta}} = \begin{cases} -\frac{k}{2z}[\zeta - \omega(z)] & \text{for } 0 \leq z \leq f \\ -\frac{k}{2f}[(2 - \frac{z}{f})\zeta - \omega(z)] & \text{for } f \leq z \leq 2f \end{cases}, \quad (\text{A12})$$

where $\frac{\partial}{\partial \bar{\zeta}}$ is called as the Wirtinger operator and defined as

$$\frac{\partial}{\partial \bar{\zeta}} = \frac{1}{2} \left(\frac{\partial}{\partial x} + i \frac{\partial}{\partial y} \right). \quad (\text{A13})$$

When $z = 2f$, Eq. (A12) becomes

$$\frac{\partial \varphi(\zeta, \bar{\zeta})}{\partial \bar{\zeta}} = \frac{k}{2f} \omega(2f). \quad (\text{A14})$$

In the complex function theory, the continuity condition in Eq. (A7) can be satisfied by antianalytic function $g(\bar{\zeta})$,

which depends only on $\bar{\zeta}$ not on ζ . The antianalytic function $g(\bar{\zeta}) = u(x, y) + iv(x, y)$ satisfies the following Cauchy-Riemann equation,

$$\frac{\partial u}{\partial x} = -\frac{\partial v}{\partial y}, \quad (\text{A15})$$

$$\frac{\partial u}{\partial y} = \frac{\partial v}{\partial x}, \quad (\text{A16})$$

where the second equation is equal to the continuity condition. Thus, we consider the antianalytic function $g(\bar{\zeta})$ as coordinate mapping at $z = 2f$, i.e., $\omega(2f) = g(\bar{\zeta})$. The stationary phase condition at $z = 2f$ is formulated as

$$\frac{\partial \varphi(\zeta, \bar{\zeta})}{\partial \bar{\zeta}} = \frac{k}{2f} g(\bar{\zeta}). \quad (\text{A17})$$

From Eq. (A17) and its complex conjugate, the solution can be expressed as a simple form given by

$$\varphi(\zeta, \bar{\zeta}) = \frac{k}{f} \text{Re} \left[\int g(\bar{\zeta}) d\bar{\zeta} \right]. \quad (\text{A18})$$

The correction phase $\Psi(\mathbf{s})$ in Eq. (A11) can be also written in complex form as

$$\Psi(\omega, \bar{\omega}) = -\varphi(\zeta_0, \bar{\zeta}_0) + \frac{k}{f} \text{Re}[\omega \bar{\zeta}_0], \quad (\text{A19})$$

where ζ_0 and $\bar{\zeta}_0$ represent the stationary phase point. Moreover, from Eqs. (A12) and (A17), the ideal conversion process of the coordinate system under propagation inside the $2f$ system can be simply represented by

$$\omega(z) = \begin{cases} \zeta + \frac{z}{f} g(\bar{\zeta}) & \text{for } 0 \leq z \leq f \\ (2 - \frac{z}{f})\zeta + g(\bar{\zeta}) & \text{for } f \leq z \leq 2f \end{cases}. \quad (\text{A20})$$

As a specific example, we consider a fractional power function $g(\bar{\zeta}) = \alpha \bar{\zeta}^{\frac{1}{N}}$, with the multiplier factor N and the scaling constant α , as an antianalytic complex function. The fractional power function is a N -valued function, and thus N number of transforming phases φ_n with integer $n = 0, \dots, N-1$ are obtained from Eq. (A18). From Eqs. (A18) and (A19), the transforming phase on the polar coordinate $\zeta = re^{i\theta}$ and the correction phase on the polar coordinate $\omega = \rho e^{i\phi}$ is given by

$$\varphi_n(r, \theta) = \frac{\alpha k N r^{1+\frac{1}{N}}}{f N + 1} \cos \left[\frac{(N+1)\theta + 2n\pi}{N} \right], \quad (\text{A21})$$

$$\Psi(\rho, \phi) = \frac{k}{f} \left(\frac{\rho}{|\alpha|} \right)^N \left[\frac{\rho \cos[(N+1)\phi]}{N+1} \right]. \quad (\text{A22})$$

Figure 7 shows the required phase distributions for the OAM doubler ($N = 2$) and tripler ($N = 3$). Moreover, by substituting $g(\bar{\zeta})$ to Eq. (A20), the ideal conversion process of the polar coordinates can be obtained, as shown in Fig. 2(b). Each coordinate mapping with the particular value of n converts the circular shape of the input OAM mode to the circular-sector shape at the different azimuthal position depending on n .

APPENDIX B: COMPLEX AMPLITUDE MODULATION BY PHASE-ONLY SPATIAL LIGHT MODULATOR

Here we describe the double-phase hologram technique to implement complex phase modulation by using a single

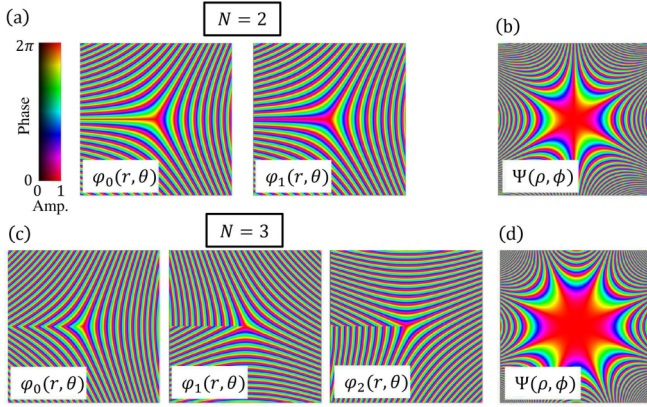


FIG. 7. Required transforming phases $\varphi_n(r, \theta)$ and the correction phase $\Psi(\rho, \phi)$ for the OAM doubler [(a), (b)] and for the OAM tripler [(c), (d)].

phase-only spatial light modulator (SLM). Let $A(\mathbf{r})e^{i\varphi(\mathbf{r})}$ be the complex amplitude modulation, where $A(\mathbf{r})$ and $\varphi(\mathbf{r})$ represent normalized amplitude and phase distribution, respectively. This modulation can be written as the sum of two-phase-only modulation,

$$A(\mathbf{r})e^{i\varphi(\mathbf{r})} = \frac{1}{2}\{e^{iP_+(\mathbf{r})} + e^{iP_-(\mathbf{r})}\}, \quad (\text{B1})$$

where two phase distributions, $P_+(\mathbf{r})$ and $P_-(\mathbf{r})$, are defined as

$$P_{\pm}(\mathbf{r}) = \varphi(\mathbf{r}) \pm \cos^{-1} A(\mathbf{r}). \quad (\text{B2})$$

In order to realize Eq. (B1) by using the single-phase-only SLM with pixel size d , we consider the following phase-only modulation,

$$e^{i\Phi(\mathbf{r})} = \Pi_+(\mathbf{r})e^{iP_+(\mathbf{r})} + \Pi_-(\mathbf{r})e^{iP_-(\mathbf{r})}, \quad (\text{B3})$$

where $\Pi_+(\mathbf{r})$ and $\Pi_-(\mathbf{r})$ are mutually complementary functions satisfying $\Pi_+(\mathbf{r}) + \Pi_-(\mathbf{r}) = 1$, and they are spatially periodic functions giving 0 or +1 with period $2d$, like a two-dimensional binary gratings [checkerboard patterns as shown in Figs. 8(a) and 8(b)]. The phase distribution $\Phi(\mathbf{r})$ in Eq. (B3) is formulated as

$$\begin{aligned} \Phi(\mathbf{r}) &= \Pi_+(\mathbf{r})P_+(\mathbf{r}) + \Pi_-(\mathbf{r})P_-(\mathbf{r}) \\ &= \varphi(\mathbf{r}) + \Pi_{\pm}(\mathbf{r})\cos^{-1} A(\mathbf{r}), \end{aligned} \quad (\text{B4})$$

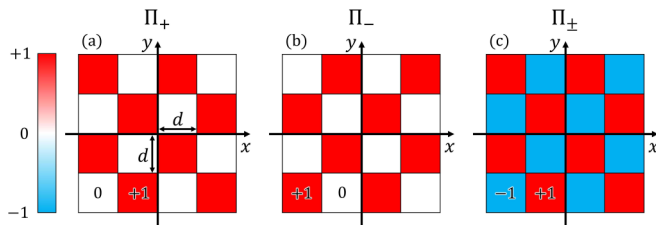


FIG. 8. Mutually complementary checkerboard patterns, (a) $\Pi_+(\mathbf{r})$, (b) $\Pi_-(\mathbf{r})$, and (c) $\Pi_{\pm}(\mathbf{r}) \equiv \Pi_+(\mathbf{r}) - \Pi_-(\mathbf{r})$.

where $\Pi_{\pm}(\mathbf{r}) \equiv \Pi_+(\mathbf{r}) - \Pi_-(\mathbf{r})$ is spatially periodic function giving +1 or -1 [see Fig. 8(c)]. The Fourier series expansion of Π_+ and Π_- are given by

$$\Pi_+(\mathbf{r}) = \frac{1}{2} + \sum_{n,m \neq 0} c_{n,m} e^{i\frac{\pi}{2}(nx+my)}, \quad (\text{B5})$$

$$\Pi_-(\mathbf{r}) = \frac{1}{2} - \sum_{n,m \neq 0} c_{n,m} e^{i\frac{\pi}{2}(nx+my)}, \quad (\text{B6})$$

where

$$c_{n,m} = \frac{\{(-1)^n - 1\}\{(-1)^m - 1\}}{2nm\pi^2}. \quad (\text{B7})$$

The Fourier transform of the phase-only modulation in Eq. (B3) with respect to $\mathbf{r} = (x, y)$ is calculated as

$$\begin{aligned} \mathcal{F}[e^{i\Phi(\mathbf{r})}] &= \sum_{j \in \{+, -\}} \mathcal{F}[\Pi_j(\mathbf{r})] * \mathcal{F}(e^{iP_j(\mathbf{r})}) \\ &= \frac{1}{2} \mathcal{F}[e^{iP_+(\mathbf{r})} + e^{iP_-(\mathbf{r})}](k_x, k_y) \\ &\quad + \sum_{n,m \neq 0} c_{n,m} \mathcal{F}[e^{iP_+(\mathbf{r})} - e^{iP_-(\mathbf{r})}] \\ &\quad \times \left(k_x - \frac{n\pi}{d}, k_y - \frac{m\pi}{d} \right), \end{aligned} \quad (\text{B9})$$

where $*$ represents convolution, k_x and k_y are two components of spatial angular frequency or wave number. Thus, the complex amplitude modulation in Eq. (B1) can be achieved by applying a spatial low-pass filter to extract the first term in from Eq. (B9) (zeroth-order diffraction component). This method is called as the double-phase hologram technique.

APPENDIX C: MEASUREMENT OF COMPLEX AMPLITUDE DISTRIBUTION

In this section, we describe about angular spectrum method to extract complex amplitude from interference pattern. Let $E_l(\mathbf{r})$ be complex amplitude of OAM mode with topological charge l . The intensity distribution $I(\mathbf{r})$ of the interference pattern between the OAM mode $E_l(\mathbf{r})$ propagating along the z direction and the reference beam $E_0(\mathbf{r})$ with slightly tilted angle Θ from z axis can be calculated as

$$\begin{aligned} I(\mathbf{r}) &\equiv |E_0(\mathbf{r})e^{ik \sin \Theta} + E_l(\mathbf{r})|^2 \\ &= |E_0(\mathbf{r})|^2 + |E_l(\mathbf{r})|^2 + \bar{E}_0(\mathbf{r})E_l(\mathbf{r})e^{-ik \sin \Theta} + \text{c.c.}, \end{aligned} \quad (\text{C1})$$

where k is the wave number, $\bar{E}_0(\mathbf{r})$ is the complex conjugate of $E_0(\mathbf{r})$, and c.c. represents complex conjugate of the previous term. From the last two terms in Eq. (C1), the Fourier transform of the interference terms are shifted by amount of $\pm k \sin \Theta$ in the angular spectrum domain. If $E_0(\mathbf{r})$ and $E_l(\mathbf{r})$ are slowly varying in spatial domain compared with the spatial angular frequency $k \sin \Theta$, we can isolate the angular spectrum corresponding to $\bar{E}_0(\mathbf{r})E_l(\mathbf{r})$. We translate the isolated interference term by $k \sin \Theta$ along the k_x axis on the angular spectrum domain and calculate the inverse Fourier transform of the translated term. Finally, the result of inverse Fourier transform is divided by the experimentally obtained amplitude

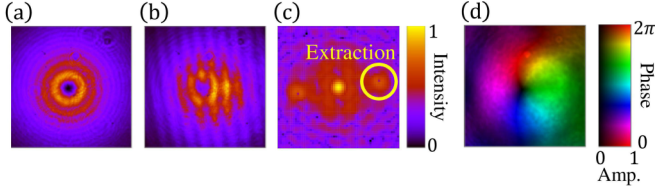


FIG. 9. (a) Intensity distribution of the OAM mode with $l = 1$. (b) Interference pattern between the OAM mode with $l = 1$ and the reference beam. (c) Fourier transform intensity of the interference pattern. (d) Optical complex amplitude extracted from one of shifted interference term in angular spectrum domain.

$|E_0|$ of the reference beam and desired complex amplitude $E_l(\mathbf{r})$ can be obtained. It is noticed that the calculated result includes the phase distribution of the reference beam $E_0(\mathbf{r})$. Thus, this method is suitable for the interference pattern with a quasiplane wave as reference beam.

Figure 9 shows a calculation example. Figure 9(a) is experimentally obtained intensity distribution of the OAM mode with $l = 1$ and Fig. 9(b) is the interference pattern between the OAM mode with $l = 1$ and the reference beam. By calculating fast Fourier transformation, we obtain the angular spectrum distribution, as shown in Fig. 9(c). By extracting one of shifted components in the angular spectrum domain and performing inverse Fourier transform, we can reconstruct the complex amplitude of the OAM mode, as shown in Fig. 9(d).

It should be noted that the band-pass filter (BPF) for extracting one of shifted components may distort the OAM spectrum (see the next section about the OAM spectrum calculation). The higher order OAM mode (higher order radial and azimuthal mode of Laguerre-Gaussian beam) includes higher spatial frequency components. Thus, the BPF in the angular spectrum domain also works as the symmetric BPF with respect to $l = 0$ in OAM spectrum domain and the amplitude of higher order OAM is underestimated. To avoid this issue, the tilted angle Θ and the bandwidth of the BPF should be as large as possible within the range where the desired complex amplitude is sufficiently isolated.

APPENDIX D: CALCULATION OF OAM SPECTRUM

Here we describe how to analyze the OAM spectrum from the complex amplitude distribution $E(r, \theta)$ with radius r and azimuthal angle θ on the polar coordinate system. Since $E(r, \theta)$ is a periodic function with respect to θ , it can be expressed as Fourier series expansion for θ as follows:

$$E(r, \theta) = \sum_{l=-\infty}^{\infty} C_l(r) e^{il\theta}, \quad (\text{D1})$$

$$C_l(r) = \frac{1}{2\pi} \int_{-\pi}^{\pi} E(r, \theta) e^{-il\theta} d\theta. \quad (\text{D2})$$

From the Parseval's theorem, the following equation is valid:

$$\frac{1}{2\pi} \int_{-\pi}^{\pi} |E(r, \theta)|^2 d\theta = \sum_{l=-\infty}^{\infty} |C_l(r)|^2. \quad (\text{D3})$$

Thus, the total intensity I_{total} is obtained by

$$\begin{aligned} I_{\text{total}} &= \int_0^{\infty} \int_{-\pi}^{\pi} |E(r, \theta)|^2 r dr d\theta \\ &= \sum_{l=-\infty}^{\infty} 2\pi \int_0^{\infty} |C_l(r)|^2 r dr, \end{aligned} \quad (\text{D4})$$

and the intensity I_l of the OAM mode with the topological charge l can be defined as

$$I_l \equiv 2\pi \int_0^{\infty} |C_l(r)|^2 r dr. \quad (\text{D5})$$

The intensity ratio or probability P_l of the OAM mode l is expressed as

$$P_l \equiv \frac{I_l}{I_{\text{total}}}. \quad (\text{D6})$$

The averaged OAM value $\langle l \rangle$ and its standard deviation δl can be calculated as

$$\langle l \rangle = \sum_l l P_l, \quad (\text{D7})$$

$$\delta l = \sqrt{\sum_l (l - \langle l \rangle)^2 P_l}. \quad (\text{D8})$$

The experimentally obtained complex amplitude is a slowly varying discrete data set. Thus, by using the interpolation function, it is possible to estimate the complex amplitude function $E(r, \theta)$ at an arbitrary point (r, θ) on the polar coordinate. In our paper, the averaged OAM $\langle l \rangle$ and its standard deviation δl is calculated within the range of $-10 \leq l \leq 10$ by using Eqs. (D7) and (D8).

APPENDIX E: ACCURACY AND EFFICIENCY EVALUATION OF OAM MULTIPLIER WITH DIFFERENT HOLOGRAM IMPLEMENTATION

Here we define efficiency of the OAM multiplier as the intensity ratio between input beam and geometrically transformed beam, without taking into account how much the desired OAM mode Nl is included in the geometrically transformed beam. On the other hand, accuracy of the OAM multiplier is defined as the intensity ratio of the desired OAM mode included in the geometrically transformed beam.

In this section, we numerically evaluate accuracy and efficiency of OAM multiplier implemented by three different holograms: the amplitude and phase hologram H_{AP} , the double-phase hologram H_{DP} , and the phase-only hologram H_{PO} , defined as

$$H_{\text{AP}}(r, \theta) \equiv A(r, \theta) e^{i\varphi(r, \theta)} = \frac{1}{N} \sum_{n=0}^{N-1} e^{i\varphi_n(r, \theta)}, \quad (\text{E1})$$

$$H_{\text{DP}}(r, \theta) \equiv e^{i\{\varphi(r, \theta) + \Pi_{\pm} \cos^{-1} A(r, \theta)\}}, \quad (\text{E2})$$

$$H_{\text{PO}}(r, \theta) \equiv e^{i\varphi(r, \theta)}, \quad (\text{E3})$$

where $\varphi_n(r, \theta)$ ($n = 0, \dots, N-1$) is defined in Eq. (A21) and $\Pi_{\pm} = (-1)^{n+m}$ with the x - and y -directional pixel numbers n and m of the hologram or the SLM is a spatially

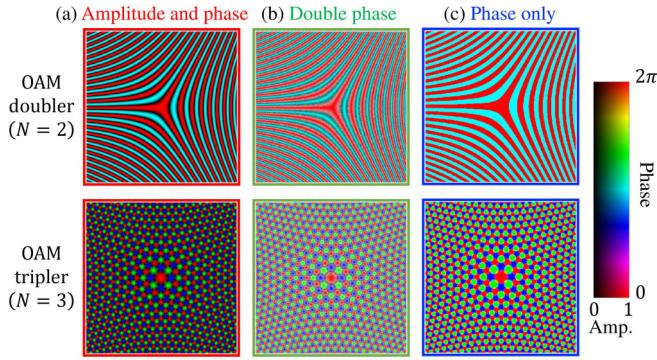


FIG. 10. Three different holograms to implement OAM doubler (upper figures) and OAM tripler (lower figures). (a) Amplitude and phase hologram $H_{AP}(r, \theta)$. (b) Double phase hologram $H_{DP}(r, \theta)$. (c) Phase-only hologram $H_{PO}(r, \theta)$.

periodic checkerboard pattern. The correction phase $\Psi(\rho, \phi)$ in Eq. (A22) is commonly used for three methods.

Figures 10(a)–10(c) show the three different holograms described above to implement the OAM doubler (upper figures) and the OAM tripler (lower figures). Figure 10(a) has both the amplitude (brightness) and the phase (hue) distributions, while Figs. 10(b) and 10(c) have only phase distribution and its amplitude is uniform.

Now we consider efficiency of the OAM multiplication implemented by three methods. First, considering the case where a plane wave is incident, the averaged transmittance T of the amplitude and phase hologram H_{AP} can be numerically calculated as follows:

$$T = \frac{1}{2\pi} \int_{-\pi}^{\pi} d\theta \lim_{R \rightarrow \infty} \frac{1}{R} \int_0^R r dr |H_{AP}(r, \theta)|^2 = \frac{1}{|N|}. \quad (\text{E4})$$

Although the actual transmittance depends on the intensity distribution of incident light, it approximately follows Eq. (E4) when the incident light has a sufficiently large beam area. Thus, the efficiency of OAM multiplication implemented by H_{AP} is almost equal to $1/|N|$, as the same with the transmittance in Eq. (E4).

Next, the transmittance of the double-phase hologram H_{DP} is unity ($|H_{DP}| = 1$), while this method has the same efficiency $1/|N|$ of OAM multiplication because it is a method for obtaining the same amplitude and phase modulation with H_{AP} as the zeroth-order diffracted light by checkerboard grating Π_{\pm} .

Unfortunately, the reduction of the efficiency for H_{AP} and H_{DP} is serious problem when we apply the OAM multiplier to quantum-optics experiment. One possible solution is the phase-only hologram H_{PO} , which can achieve higher efficiency than the other two methods, although extra noise distribution is generated outside the desired output complex amplitude distribution, as shown below. Actually, in Ref. [42], the OAM multiplier is realized by the phase-only hologram.

In what follows, we evaluate accuracy and efficiency of the OAM doubler and the OAM tripler using perfect optical vortex (perfect OV) beam with the same beam radius in different OAM mode l as input light field. The complex amplitude

distribution $E(r, \theta)$ of perfect OV beam can be defined as

$$E(r, \theta) = A \exp \left[-\frac{(r - r_0)^2}{2w_0^2} \right] e^{il\theta}, \quad (\text{E5})$$

where r_0 and w_0 are the radius and the width of the ring-shape distribution, respectively, and A is the amplitude.

Figure 11 shows cross-sectional intensity distributions and complex amplitude distributions of the input perfect OV [Fig. 11(a)], output of the OAM doubler [Fig. 11(b)], and output of the OAM tripler [Fig. 11(c)], with the range of input OAM mode number $0 \leq l \leq 2$, the beam radius $r_0 = 3$ mm, the ring width $w_0 = 1$ mm, the focal length of the lens $f = 200$ mm, and the wavelength $\lambda = 633$ nm. The scaling constant is $\alpha = 1.1 \times 10^{-2} \text{ m}^{1/2}$ and $\alpha = 4.2 \times 10^{-3} \text{ m}^{2/3}$ for the OAM doubler and the OAM tripler, respectively, so that the beam radius ρ_0 of the output complex amplitude becomes constant value, i.e., $\rho_0 = \alpha r_0^{1/N} = 0.2r_0$.

The first, second, and the third rows in Figs. 11(b) and 11(c) correspond to the OAM multiplier implemented by the three different holograms H_{AP} , H_{DP} , and H_{PO} , respectively. From the complex amplitude distribution within the radius $R = 1.84$ mm, there seems to be no significant difference between the OAM multiplier implemented by three different methods. However, from the cross-sectional intensity distributions in dB scale within the radius $2.5R = 4.6$ mm (the leftmost figures in Fig. 11), it is clear that the amplitude and phase hologram H_{AP} has the least noise and the second least is the double-phase hologram H_{DP} . When using the phase-only hologram H_{PO} , unnecessary noise distribution is generated outside the desired ring-shaped distribution. However, its efficiency is over 80% (within the radius R), which is a significant advantage over the efficiency of the other two methods, which are limited by $1/|N|$.

Figure 12 shows a variation of maximum probability of desired output OAM with respect to the input OAM mode l , for the OAM doubler [Fig. 12(a)] and OAM tripler [Fig. 12(b)]. Here we calculate the geometric transformation by Fourier transform of input OAM mode multiplied with the hologram, followed by the phase correction by $\Psi(\rho, \phi)$. Within the radius of R , the three methods have almost the same maximum probabilities. However, within the radius of $2.5R$, the maximum probability of the phase-only hologram H_{PO} is reduced because the unnecessary distribution outside the desired ring shape has random phase through the correction phase $\Psi(\rho, \phi)$. Thus, when we use the phase-only hologram, it is necessary to remove the unnecessary distribution with an appropriate pinhole. Even in the case of the double-phase hologram, it is necessary to extract zeroth-order diffracted light by a appropriate pinhole. However, in the case of the double-phase hologram, the distance between the unnecessary and the necessary components is determined by the period of the checkerboard grating Π_{\pm} , whereas in the case of the phase-only hologram, the location of the unnecessary component varies with the beam diameter of the incident light. Despite these drawbacks of the phase-only hologram, its higher efficiency is significantly attractive, in particular, for the quantum-optics experiment.

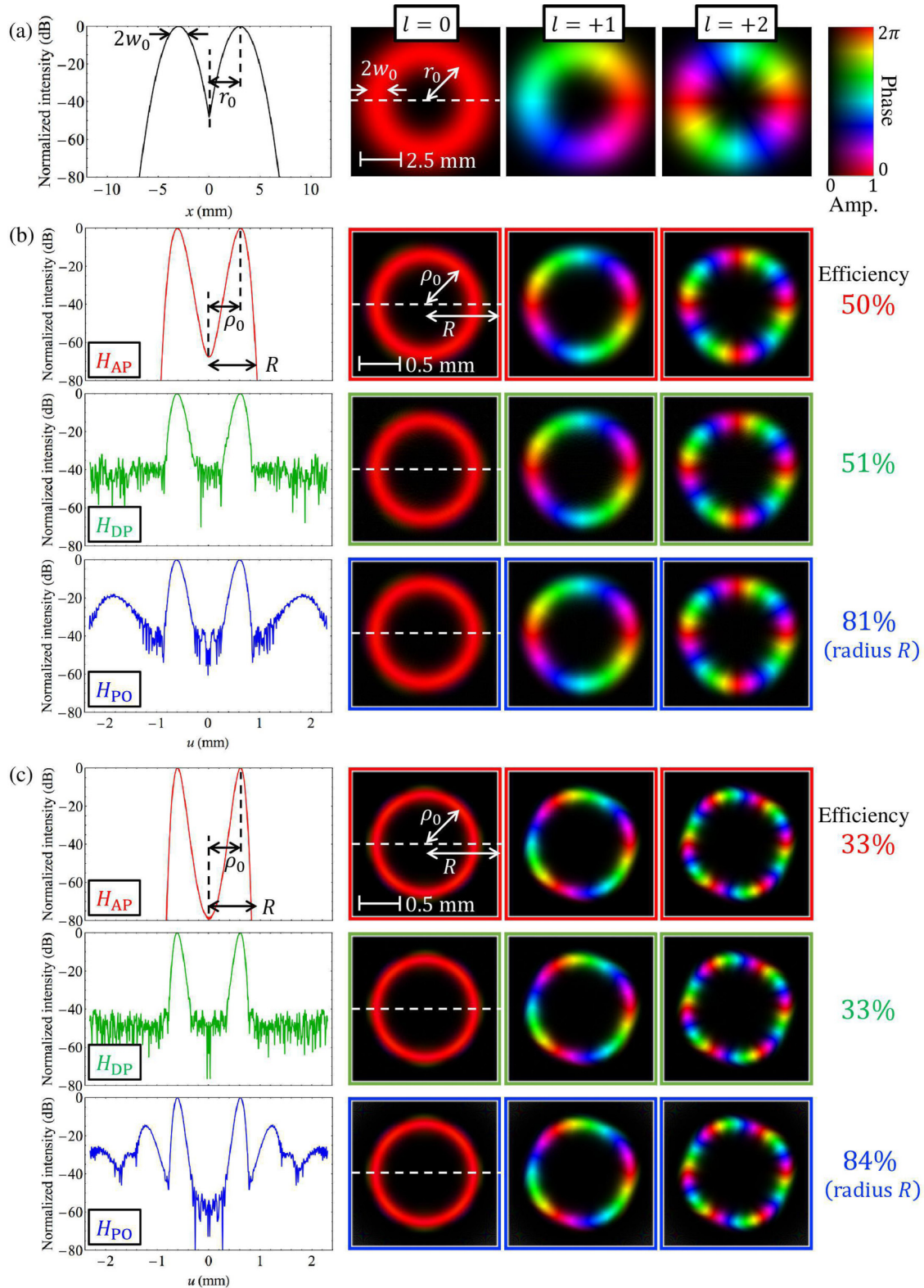


FIG. 11. Cross-sectional intensity distributions and complex amplitude distributions of (a) input perfect optical vortex (OV) beams with the mode $0 \leq l \leq 2$, (b) output of the OAM doubler, and (c) output of the OAM tripler. The leftmost figures show the cross-sectional normalized intensity distribution along white dotted line of the second column in decibels (dB) for the OAM mode. The OAM doubler ($N = 2$) and tripler ($N = 3$) are implemented by using the three different methods: the amplitude-phase hologram H_{AP} , the double-phase hologram H_{DP} , and the phase-only hologram H_{PO} . The rightmost numbers show the efficiency of OAM multiplication implemented by three methods. The scaling constant α of the OAM doubler and tripler are $1.1 \times 10^{-2} \text{ m}^{1/2}$ and $4.2 \times 10^{-3} \text{ m}^{2/3}$, respectively, beam radius $r_0 = 3 \text{ mm}$, ring width $w_0 = 1 \text{ mm}$, focal length of lens $f = 200 \text{ mm}$, and wavelength $\lambda = 633 \text{ nm}$.

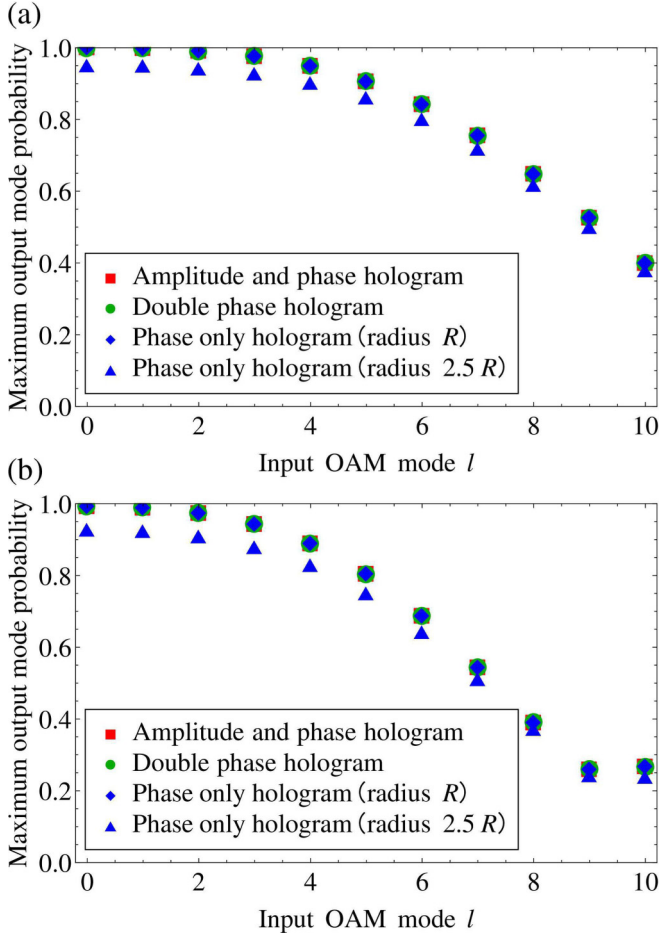


FIG. 12. Maximum probability of desired output mode for (a) OAM doubler and (b) OAM tripler implemented by H_{AP} (red square), H_{DP} (green disk), and H_{PO} [blue diamond (radius R) and blue triangle (radius $2.5R$)] with respect to input OAM mode l . The parameters r_0 , w_0 , f , λ , and α are the same as in Fig. 11.

In the next section, we discuss in detail the variation of the maximum probability of the desired OAM mode with respect to the input OAM mode l .

APPENDIX F: ACCURACY EVALUATION OF OAM MULTIPLIER WITH RESPECT TO MULTIPLE NUMBER AND INPUT BEAM PARAMETERS

In this section, we discuss in detail how accuracy or maximum probability of the desired output OAM mode in the OAM multiplier varies with multiplier number N and input beam parameters (mode number l , beam radius r_0 , and beam width w_0). In Appendix A, we considered $\varphi_n(\mathbf{r})$ and $(k/f)\mathbf{s} \cdot \mathbf{r}$ in Eq. (A3) as rapidly oscillating phase terms to apply the stationary phase method. However, when input OAM mode l or/and ratio r_0/w_0 become large, the complex amplitude of the input beam $E_{in}(\mathbf{r})$ includes rapidly oscillating phase terms, which distort the output complex amplitude.

There are two main factors of distortion in the output complex amplitude due to the rapidly oscillating term in the input beam. The first one is coordinate mapping distortion

between $\mathbf{r} = (x, y)$ and $\mathbf{s} = (u, v)$, formulated in Eq. (A6). The second one is amplitude distortion inversely proportional to $\sqrt{|\varphi_{xx}\varphi_{yy} - \varphi_{xy}^2|}$ in Eq. (A9). From these two factors, we can derive the required condition for negligible distortion. In what follows, we use the amplitude and phase hologram $H_{AP}(r, \theta)$ to implement the OAM multiplier.

The input OAM mode $E_{in}(\mathbf{r})$ can be decomposed to two phase-only distribution as follows,

$$E_{in}(\mathbf{r}) = \frac{E_{max}}{2} \{e^{iQ_+(\mathbf{r})} + e^{iQ_-(\mathbf{r})}\}, \quad (F1)$$

where E_{max} is the maximum value of $|E_{in}(\mathbf{r})|$ and $Q_{\pm}(\mathbf{r})$ is defined as

$$Q_{\pm}(\mathbf{r}) \equiv \arg E_{in}(\mathbf{r}) \pm \cos^{-1} \frac{|E_{in}(\mathbf{r})|}{E_{max}}. \quad (F2)$$

Now we consider the perfect OV in Eq. (E5) as $E_{in}(\mathbf{r})$ and the phase term $Q_{\pm}(\mathbf{r})$ becomes

$$Q_{\pm}(r, \theta) = l\theta \pm \text{sign}(r - r_0) \cos^{-1} \left[e^{-\frac{(r-r_0)^2}{2w_0^2}} \right], \quad (F3)$$

where $\text{sign}(x) \equiv x/|x|$ is added so that the differential function of $Q_{\pm}(r, \theta)$ becomes continuous. The first rows in Figs. 13(a) and 13(b) show complex amplitude distributions of input perfect OV with $l = 10$ and $l = 0$, respectively, and their decomposition to two phase-only distributions Q_+ and Q_- .

Here we define the total phase term $\tilde{\varphi}^{\pm}(r, \theta)$ as

$$\tilde{\varphi}^{\pm}(r, \theta) \equiv \varphi_n(r, \theta) + Q_{\pm}(r, \theta). \quad (F4)$$

From Eq. (A6), coordinate mapping between (u, v) and (r, θ) can be written as

$$\begin{pmatrix} u \\ v \end{pmatrix} = \frac{f}{k} \nabla \tilde{\varphi}^{\pm}(r, \theta) \quad (F5)$$

$$= \alpha r^{\frac{1}{N}} \begin{pmatrix} \cos \frac{\theta + 2n\pi}{N} \\ -\sin \frac{\theta + 2n\pi}{N} \end{pmatrix} \pm \beta(r) \begin{pmatrix} \cos[\theta \pm \chi(r)] \\ \sin[\theta \pm \chi(r)] \end{pmatrix}, \quad (F6)$$

where $h(x)$, $\beta(r)$, and $\chi(r)$ are defined as

$$h(x) = \frac{|x|}{\sqrt{e^{x^2} - 1}}, \quad (F7)$$

$$\beta(r) = \frac{f}{kr} \sqrt{l^2 + \left\{ \frac{r}{w_0} h\left(\frac{r-r_0}{w_0}\right) \right\}^2}, \quad (F8)$$

$$\chi(r) = \tan^{-1} \left[\frac{lw_0}{r} h\left(\frac{r-r_0}{w_0}\right)^{-1} \right]. \quad (F9)$$

The second term in Eq. (E5) causes coordinate mapping distortion in output complex amplitude distribution.

Equation (E5) is parametric equation of a trochoid (hypotrochoid for $N > 0$ and epitrochoid for $N < 0$), which is a curve traced by a point with distance of $\alpha r^{\frac{1}{N}}$ from the center of a circle with radius of $N\beta(r)$ rolling around the inside (for hypotrochoid) or outside (for epitrochoid) of a fixed circle with radius $(N+1)\beta(r)$, rotated by an angle of $\pm \frac{\chi(r)}{N+1}$ [see the second rows in Figs. 13(a) and 13(b)]. When $r_0/w_0 \ll l$, $\chi(r_0) = \pi/2$, and two phase-only distributions are geometrically transformed into almost the same distorted shapes as shown in the second row of Fig. 13(a), while when $r_0/w_0 \gg l$, they are transformed into different two shapes

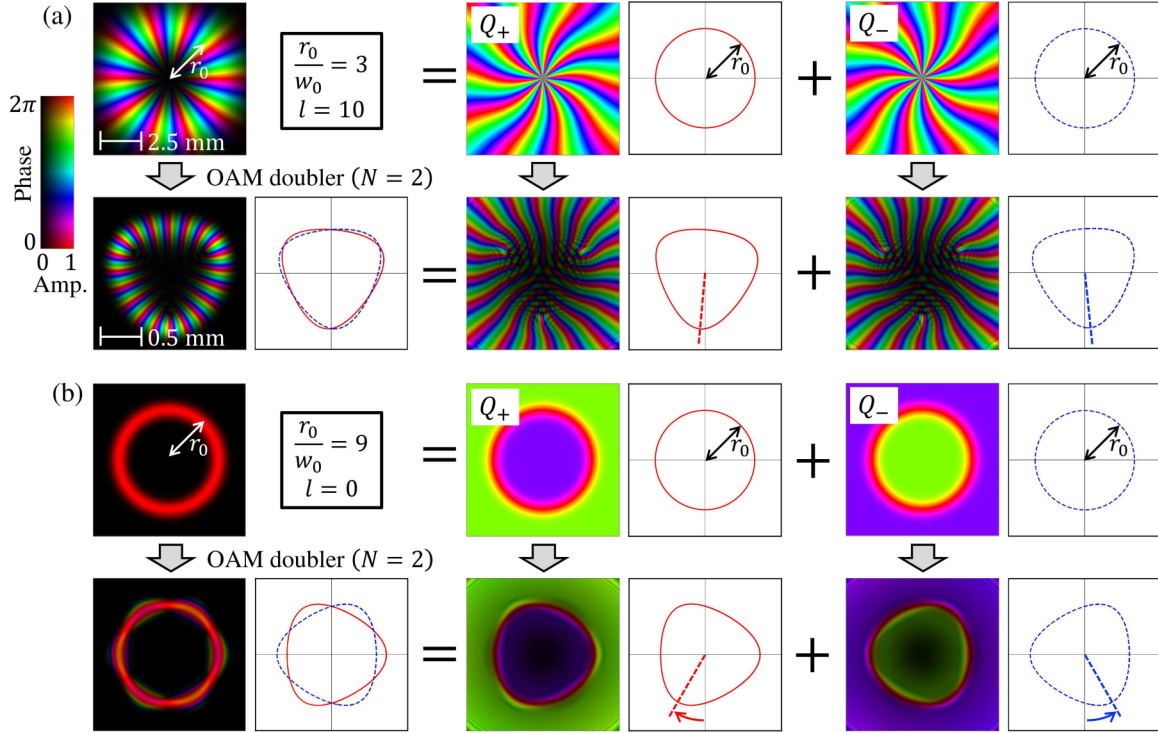


FIG. 13. Complex amplitude distortion of OAM doubler ($N = 2$) implemented by the amplitude and phase hologram H_{AP} , (a) when $r_0/w_0 < l$ and (b) when $r_0/w_0 > l$. The complex amplitude of input perfect OV can be decomposed to two phase-only distributions, as shown in the first and the third rows. When $r_0/w_0 < l$, two phase-only distributions are geometrically transformed into almost the same distorted shapes, while when $r_0/w_0 > l$, they are transformed into different two shapes, which are oppositely rotated by the angle of $\chi(r)/(N + 1)$.

oppositely rotated by the angle of $\chi(r)/(N + 1)$, as shown in the second row of Fig. 13(b).

When $r = r_0$, the condition that the second term becomes negligible compared to the first term in Eq. (E5) is simply

written by

$$\alpha r_0^{\frac{1}{N}} \gg \frac{f}{kr_0} \sqrt{l^2 + \gamma^2}, \quad (\text{F10})$$

where we used $h(0) = 1$ and $\gamma \equiv \frac{r_0}{w_0}$. By reformulating Eq. (F10), we can obtain the following condition:

$$\Lambda_N(r_0) \equiv \frac{f\lambda}{\alpha r_0^{\frac{1}{N}}} = \frac{f\lambda}{\rho_0} \ll \frac{2\pi r_0}{\sqrt{l^2 + \gamma^2}}, \quad (\text{F11})$$

where $\rho_0 \equiv \alpha r_0^{\frac{1}{N}}$ is the radius when ideal circular sector transformation is applied to the radius r_0 and $\Lambda_N(r_0)$ is minimum phase period of amplitude and phase hologram H_{AP} at the radius r_0 for N -fold OAM multiplier. The condition in Eq. (F11) means that the period $\Lambda_N(r_0)$ of the hologram should be much smaller than the phase variation of the input perfect OV, as shown in Fig. 14. From Eq. (F11), the condition for negligible distortion seems to be independent of the multiplier number N when the output beam radius ρ_0 is constant. However, as shown below, the amplitude distortion related to the second-order differential of the phase function does depend on N .

Next, we calculate the amplitude distortion factor in Eq. (A9), which can be simply calculated by using complex variables $\zeta = x + iy$ and the Wirtinger operator in Eq. (A13)

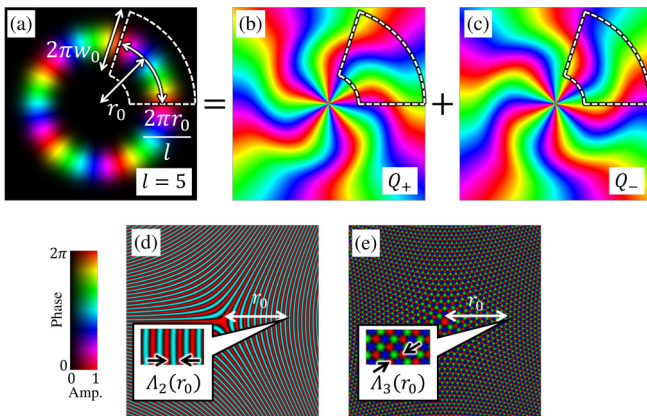


FIG. 14. (a) Complex amplitude of input perfect OV with the mode $l = +5$, $r_0 = 3$ mm, and $r_0/w_0 = 6$. [(b), (c)] Two phase-only distributions Q_+ and Q_- generating input perfect OV. [(d), (e)] Amplitude and phase hologram $H_{AP}(r, \theta)$ for OAM doubler ($N = 2$) and OAM tripler ($N = 3$), where $\Lambda_N(r_0)$ shows 2π phase period of the hologram at the radius r_0 for the multiplier number N . The parameters f , λ , and α are the same as in Fig. 11.

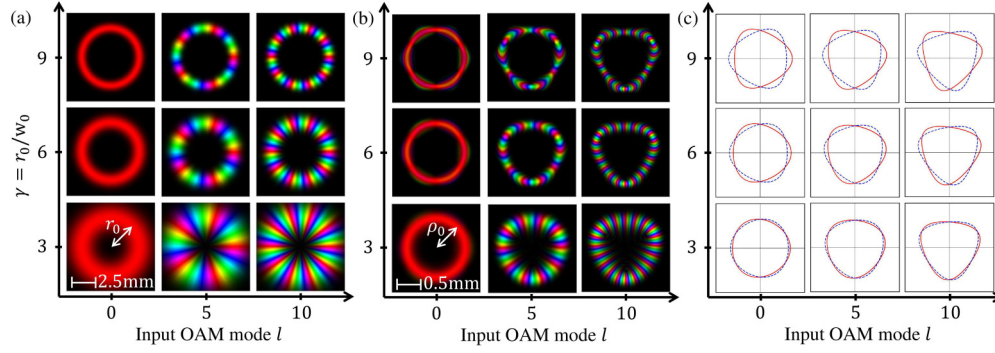


FIG. 15. Complex amplitude distortion of OAM doubler ($N = 2$) with respect to input OAM mode l and ratio γ between radius r_0 and width w_0 of the input perfect OV beam. (a) Complex amplitude of the input perfect OV. (b) Output complex amplitude distribution of the OAM doubler. (c) Coordinate mapping distortion of input radius r_0 .

as follows:

$$\tilde{\varphi}_{xx}^{\pm} \tilde{\varphi}_{yy}^{\pm} - \tilde{\varphi}_{xy}^{\pm 2} = 4(\tilde{\varphi}_{\xi\xi}^{\pm 2} - \tilde{\varphi}_{\xi\xi}^{\pm} \tilde{\varphi}_{\xi\xi}^{\pm}) \quad (\text{F12})$$

$$= \left\{ \frac{h_{\pm}(r)}{2w_0 r} \right\}^2 - \frac{1}{r^4} \left| \frac{\alpha k}{fN} r^{1+\frac{1}{N}} e^{i\frac{(N+1)\theta+2\pi n}{N}} + il \pm \frac{r}{2w_0} h_{\pm}(r) \right|^2, \quad (\text{F13})$$

where $h_{\pm}(r)$ is defined as

$$h_{\pm}(r) \equiv \frac{r}{w_0} h' \left(\frac{r-r_0}{w_0} \right) \pm h \left(\frac{r-r_0}{w_0} \right), \quad (\text{F14})$$

with $h'(x) \equiv \frac{dh(x)}{dx}$. Here we note that $h_{\pm}(r_0) = \pm 1$. The amplitude distortion term depending on the azimuthal angle θ in Eq. (F13) spoils the desired OAM spectrum. The condition that the θ -dependent term becomes negligible in Eq. (F13) at $r = r_0$ is written by

$$\frac{\alpha k}{f|N|} r_0^{1+\frac{1}{N}} \gg \sqrt{l^2 + \left(\frac{\gamma}{2}\right)^2}. \quad (\text{F15})$$

By reformulating Eq. (F15), we can obtain the following condition:

$$\Lambda_N(r_0) \equiv \frac{f\lambda}{\alpha r_0^{\frac{1}{N}}} = \frac{f\lambda}{\rho_0} \ll \frac{2\pi r_0}{|N| \sqrt{l^2 + \left(\frac{\gamma}{2}\right)^2}}. \quad (\text{F16})$$

By comparing Eqs. (F11) and (F16), the second one is a stronger condition than the first one, when $|N| \geq 2$. Moreover, as an additional condition, resolution (or pixel size) δs of the hologram or the SLM should be much smaller than the phase period $\Lambda_N(r_0)$. Thus, the final result of required condition for negligible distortion is given by

$$\delta s \ll \Lambda_N(r_0) = \frac{f\lambda}{\rho_0} \ll \frac{2\pi r_0}{|N| \sqrt{l^2 + \left(\frac{\gamma}{2}\right)^2}}. \quad (\text{F17})$$

Thus, the focal length f , the wavelength λ , and the output beam radius ρ_0 should be selected to satisfy Eq. (F17) for a given resolution δs of the hologram or the SLM. To increase the nondistortion range of the multiplier number N and the input OAM mode l , the radius r_0 should be increased.

However, the maximum beam radius is normally limited by the manufacturable hologram size or the active area size of the SLM. For example, when $r_0 = 3$ mm, $\rho_0 = 0.2r_0 = 0.6$ mm, the focal length $f = 200$ mm, and the wavelength $\lambda = 633$ nm, the required condition for l and γ is given by

$$\sqrt{l^2 + \left(\frac{\gamma}{2}\right)^2} \ll \frac{89.3}{|N|}. \quad (\text{F18})$$

Figure 15 shows simulation results of complex amplitude distortion of OAM doubler. As the value of l or/and $\gamma = r_0/w_0$ becomes larger, the input perfect OV in Fig. 15(a) becomes more distorted, as shown in Fig. 15(b), due to the coordinate mapping distortion [see Fig. 15(c)] and amplitude distortion [see the stronger intensity on the corner of the distorted shape in Fig. 15(b)]. Figure 16 shows variation of maximum probability of desired output OAM mode with respect to input OAM mode l and ratio $\gamma = r_0/w_0$ for OAM doubler and tripler. A contour line of the probability in Fig. 16 can be qualitatively described by the condition in Eq. (F15).

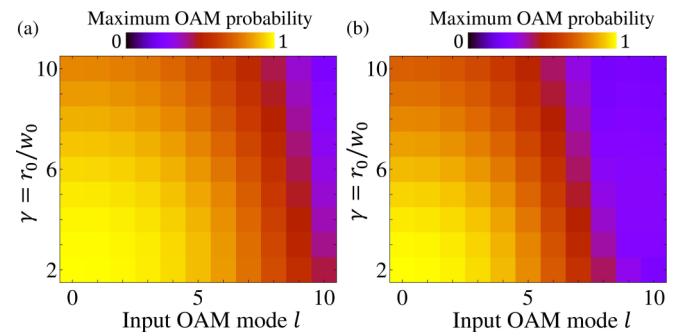


FIG. 16. Variation of maximum probability of desired output OAM mode with respect to input OAM mode l and ratio γ between radius r_0 and width w_0 of the input perfect OV beam for (a) OAM doubler and (b) OAM tripler.

- [1] L. Allen, M. W. Beijersbergen, R. J. C. Spreeuw, and J. P. Woerdman, *Phys. Rev. A* **45**, 8185 (1992).
- [2] H. Rubinsztein-Dunlop, A. Forbes, M. V. Berry, M. R. Dennis, D. L. Andrews, M. Mansuripur, C. Denz, C. Alpmann, P. Banzer, T. Bauer *et al.*, *J. Opt.* **19**, 013001 (2016).
- [3] G. Gibson, J. Courtial, M. J. Padgett, M. Vasnetsov, V. Pas'ko, S. M. Barnett, and S. Franke-Arnold, *Opt. Express* **12**, 5448 (2004).
- [4] J. Wang, J.-Y. Yang, I. M. Fazal, N. Ahmed, Y. Yan, H. Huang, Y. Ren, Y. Yue, S. Dolinar, M. Tur *et al.*, *Nat. Photon.* **6**, 488 (2012).
- [5] S. W. Hell and J. Wichmann, *Opt. Lett.* **19**, 780 (1994).
- [6] N. Simpson, L. Allen, and M. Padgett, *J. Mod. Opt.* **43**, 2485 (1996).
- [7] A. Mair, A. Vaziri, G. Weihs, and A. Zeilinger, *Nature (London)* **412**, 313 (2001).
- [8] R. Fickler, R. Lapkiewicz, W. N. Plick, M. Krenn, C. Schaeff, S. Ramelow, and A. Zeilinger, *Science* **338**, 640 (2012).
- [9] S. Gröblacher, T. Jennewein, A. Vaziri, G. Weihs, and A. Zeilinger, *New J. Phys.* **8**, 75 (2006).
- [10] M. Mafu, A. Dudley, S. Goyal, D. Giovannini, M. McLaren, M. J. Padgett, T. Konrad, F. Petruccione, N. Lütkenhaus, and A. Forbes, *Phys. Rev. A* **88**, 032305 (2013).
- [11] M. Beijersbergen, R. Coerwinkel, M. Kristensen, and J. Woerdman, *Opt. Commun.* **112**, 321 (1994).
- [12] W. Harm, S. Bernet, M. Ritsch-Marte, I. Harder, and N. Lindlein, *Opt. Express* **23**, 413 (2015).
- [13] N. Heckenberg, R. McDuff, C. Smith, and A. White, *Opt. Lett.* **17**, 221 (1992).
- [14] T. Ando, Y. Ohtake, N. Matsumoto, T. Inoue, and N. Fukuchi, *Opt. Lett.* **34**, 34 (2009).
- [15] L. Marrucci, C. Manzo, and D. Paparo, *Phys. Rev. Lett.* **96**, 163905 (2006).
- [16] L. Marrucci, *J. Nanophotonics* **7**, 078598 (2013).
- [17] M. Mansuripur, A. R. Zakharian, and E. M. Wright, *Phys. Rev. A* **84**, 033813 (2011).
- [18] H. Kobayashi, K. Nonaka, and M. Kitano, *Opt. Express* **20**, 14064 (2012).
- [19] N. Yu, P. Genevet, M. A. Kats, F. Aieta, J.-P. Tetienne, F. Capasso, and Z. Gaburro, *Science* **334**, 333 (2011).
- [20] Z. Zhao, J. Wang, S. Li, and A. E. Willner, *Opt. Lett.* **38**, 932 (2013).
- [21] E. Karimi, S. A. Schulz, I. De Leon, H. Qassim, J. Upham, and R. W. Boyd, *Light Sci. Appl.* **3**, e167 (2014).
- [22] A. E. Willner, L. Li, G. Xie, Y. Ren, H. Huang, Y. Yue, N. Ahmed, M. J. Willner, A. J. Willner, Y. Yan *et al.*, *Photon. Res.* **4**, B5 (2016).
- [23] J. C. García-Escartín and P. Chamorro-Posada, *Phys. Rev. A* **78**, 062320 (2008).
- [24] K. Dholakia, N. B. Simpson, M. J. Padgett, and L. Allen, *Phys. Rev. A* **54**, R3742(R) (1996).
- [25] N. V. Bloch, K. Shemer, A. Shapira, R. Shiloh, I. Juwiler, and A. Arie, *Phys. Rev. Lett.* **108**, 233902 (2012).
- [26] G. Gariepy, J. Leach, K. T. Kim, T. J. Hammond, E. Frumker, R. W. Boyd, and P. B. Corkum, *Phys. Rev. Lett.* **113**, 153901 (2014).
- [27] V. Potoček, F. M. Miatto, M. Mirhosseini, O. S. Magaña-Loaiza, A. C. Liapis, D. K. L. Oi, R. W. Boyd, and J. Jeffers, *Phys. Rev. Lett.* **115**, 160505 (2015).
- [28] Z. Zhao, Y. Ren, G. Xie, L. Li, Y. Yan, N. Ahmed, Z. Wang, C. Liu, A. J. Willner, S. Ashrafi *et al.*, *APL Photon.* **1**, 090802 (2016).
- [29] G. C. G. Berkhout, M. P. J. Lavery, J. Courtial, M. W. Beijersbergen, and M. J. Padgett, *Phys. Rev. Lett.* **105**, 153601 (2010).
- [30] M. N. O'Sullivan, M. Mirhosseini, M. Malik, and R. W. Boyd, *Opt. Express* **20**, 24444 (2012).
- [31] Y. Wen, I. Chremmos, Y. Chen, J. Zhu, Y. Zhang, and S. Yu, *Phys. Rev. Lett.* **120**, 193904 (2018).
- [32] C. Hsueh and A. Sawchuk, *Appl. Opt.* **17**, 3874 (1978).
- [33] O. Mendoza-Yero, G. Mínguez-Vega, and J. Lancis, *Opt. Lett.* **39**, 1740 (2014).
- [34] O. Bryngdahl, *J. Opt. Soc. Am. A* **64**, 1092 (1974).
- [35] O. Bryngdahl, *Opt. Commun.* **10**, 164 (1974).
- [36] M. Stuff and J. Cederquist, *J. Opt. Soc. Am. A* **7**, 977 (1990).
- [37] J. Cederquist and A. M. Tai, *Appl. Opt.* **23**, 3099 (1984).
- [38] A. E. Bereznyi and I. N. Sissakian, *Comput. Opt.* **2**, 115 (1990).
- [39] T. W. Clark, R. F. Offer, S. Franke-Arnold, A. S. Arnold, and N. Radwell, *Opt. Express* **24**, 6249 (2016).
- [40] N. Radwell, R. F. Offer, A. Selyem, and S. Franke-Arnold, *J. Opt.* **19**, 095605 (2017).
- [41] M. Takeda, H. Ina, and S. Kobayashi, *J. Opt. Soc. Am.* **72**, 156 (1982).
- [42] G. Ruffato, M. Massari, and F. Romanato, *Light Sci. Appl.* **8**, 113 (2019).